

Nature of the DLA towards Q 0528–250[★]: High pressure and strong UV field revealed by excitation of C i, H₂ and Si ii

S. A. Balashev,^{1†} C. Ledoux,² P. Noterdaeme,³ R. Srianand,⁴ P. Petitjean,³
and N. Gupta⁴

¹ *Ioffe Institute, Polytekhnicheskaya 26, 194021 Saint-Petersburg, Russia*

² *European Southern Observatory, Alonso de Córdova 3107, Vitacura, Casilla 19001, Santiago, Chile*

³ *Institut d’Astrophysique de Paris, CNRS-SU, UMR 7095, 98bis boulevard Arago, 75014 Paris, France*

⁴ *Inter-University Centre for Astronomy and Astrophysics, Pune University Campus, Ganeshkhind, Pune 411007, India*

Accepted 2020 July 15. Received 2020 June 28; in original form 2020 March 6

ABSTRACT

We present the detection of excited fine-structure energy levels of singly-ionized silicon and neutral carbon associated with the proximate damped Lyman- α system at $z_{\text{abs}} = 2.811$ towards Q 0528–250. This absorber has an apparent relative velocity that is inconsistent with the Hubble flow indicating motion along the line-of-sight towards the quasar, i.e., $z_{\text{abs}} > z_{\text{em}}$. We measure the metallicity of the system to be $[\text{Zn}/\text{H}] = -0.68 \pm 0.02$. Using the relative populations of the fine-structure levels of Si II and C I, as well as the populations of H₂ rotational levels, we constrain the physical conditions of the gas. We derive hydrogen number densities of $n_{\text{H}} = 190_{-50}^{+70} \text{ cm}^{-3}$ and $260_{-20}^{+30} \text{ cm}^{-3}$ in two velocity components where both C I and H₂ are detected. Taking into account the kinetic temperature in each component, $\sim 150 \text{ K}$, we infer high values of thermal pressure in the cold neutral medium probed by the observations. The strengths of the UV field in Draine’s unit are $I_{\text{UV}} = 10_{-3}^{+5}$ and 14_{-3}^{+3} in each of these two components, respectively. Such enhanced UV fluxes and thermal pressure compared to intervening DLAs are likely due to the proximity of the quasar. The typical size of the absorber is $\sim 10^4$ a.u. Assuming the UV flux is dominated by the quasar, we constrain the distance between the quasar and the absorber to be $\sim 150 - 200 \text{ kpc}$. This favours a scenario where the absorption occurs in a companion galaxy located in the group where the quasar-host galaxy resides. This is in line with studies in emission that revealed the presence of several galaxies around the quasar.

Key words: cosmology: observations – quasar: absorption lines – ISM: clouds, molecules

1 INTRODUCTION

Quasars are active phases of super-massive black holes that reside in the core of galaxies and play a major role in the formation and evolution of galaxies through so-called feedback processes. Quasars are fed with gas principally released through galaxy interactions and/or mergers. The rate of such processes is significantly enhanced in denser environments and therefore quasar hosts are believed to be pre-

dominantly located in massive galaxy groups. The gas in these groups can be studied in absorption in the spectra of quasars that may either be group members or located in the background. Of particular interest are the proximate DLAs (i.e., PDLAs), i.e., damped Lyman- α systems (DLAs; with $\log N(\text{H I}) \gtrsim 20$) associated with the quasar host galaxy and/or its environment. These absorbers allow to explore the physical conditions of high column-density gas under the influence of quasar feedback.

Based on the CORALS survey, Ellison et al. (2002) reported a factor of ~ 4 excess of PDLAs compared to intervening DLAs. Prochaska et al. (2008) found a factor of ~ 2 excess at redshifts $z \sim 3$ from the Sloan Digital Sky Survey (SDSS) data release-5, but no statistically significant excess

[★] Based on data collected at the European Southern Observatory under ESO programmes 66.A-0594, 68.A-0600, 68.A-0106, and 082.A-0087.

[†] E-mail: s.balashev@gmail.com

at $z < 2.5$ or $z > 3.5$. Additionally, [Noterdaeme et al. \(2019\)](#) found that H_2 -selected PDLAs with $z > 3$ show an excess by factors of 4–5¹ compared to intervening DLAs selected in the same way. The discrepancy between these studies may be due to the complex spectral-line profile in the $\text{Ly}\alpha$ region for a large fraction of PDLAs (e.g., [Hennawi et al. 2009](#); [Finley et al. 2013](#)), caused by strong residual $\text{Ly}\alpha$ emission not absorbed by the DLA. Such PDLAs are called coronagraphic. PDLA searches based on the standard assumption of complete $\text{Ly}\alpha$ absorption troughs may miss a large fraction of such systems.

In extreme cases, the extent of the neutral gas clouds producing the DLA is smaller than the size of the Broad Line Region (BLR) of the quasar. The leaking broad $\text{Ly}\alpha$ emission may then fill the DLA trough, resulting in the formation of a "ghostly" DLA in the quasar spectrum ([Jiang et al. 2016](#); [Fathivavsari et al. 2017](#)). Usually, coronagraphic DLAs exhibit relatively high excitation of fine-structure energy levels of Si II, C I, and/or O I. Based on the observation of a direct relation between the strength of leaking $\text{Ly}\alpha$ emission and fine-structure excitation of metal species, [Fathivavsari et al. \(2018\)](#) suggested that systems with strong $\text{Ly}\alpha$ emission (and therefore with probably less covering of the $\text{Ly}\alpha$ emitting region) could be denser and located closer to the AGN. Such DLAs could be subject to mechanical compression of the gas and/or enhanced incident UV fluxes, both of which can contribute to the excitation of the above-mentioned fine-structure levels.

Though these distinct classes of PDLAs are now routinely identified in SDSS spectra, the spectral resolution of the SDSS ($R \sim 2000$) is insufficient to study them in detail. Medium- to high-resolution observations are required to exploit the information encoded in the fine-structure levels of metal species and/or H_2 rotational levels, which can then be used to infer the excitation and physical conditions of the gas in these harsh environments. Unfortunately, follow-up observations are difficult as most of the corresponding quasars are faint and, to date, only a few high-resolution spectra of PDLAs towards relatively bright quasars are available. Among those, the DLA system at $z_{\text{abs}} = 2.811$ towards Q 0528–250 stands out as a unique absorber for having a redshift higher than that of the quasar by several thousands of km s^{-1} , suggesting proximity to the quasar, together with the detection of prominent H_2 lines.

In this paper, we focus on the method to constrain the fine-structure excitation of the Si II and C I ground states and analyse the physical conditions of the absorbing gas. In Sect. 2, we summarize previous studies of this DLA. Using high-quality VLT spectra retrieved from the ESO archive (see [Klimenko et al. 2015](#)), we confirm the presence of C I and C I* and present new detection of Si II* and C I** in this system (Sect. 3). Coupled with a study of H_2 rotational excitation, this allows us to estimate the hydrogen number density and UV flux in the cold neutral medium associated with the H_2 components and to constrain the physical distance between the DLA and the quasar (Sect. 4). We dis-

cuss the implications of this result in Sect. 5 and conclude in Sect. 6.

2 PREVIOUS STUDIES OF Q 0528–250

The DLA system at $z_{\text{abs}} = 2.811$ towards Q 0528–250 was identified by [Jauncey et al. \(1978\)](#) from follow-up low-resolution optical spectroscopy ($\Delta\lambda=10 \text{ \AA}$) of radio sources from the Parkes 2.7 GHz sample. [Jauncey et al.](#) did not detect any emission line in this spectrum, but subsequent observations by [Smith et al. \(1979\)](#) revealed Si IV and C IV emission lines at $z = 2.765 \pm 0.01$, i.e., significantly lower than the DLA redshift, which indicated that the absorber is located in the vicinity of the quasar. A higher resolution spectrum ($\Delta\lambda=2 \text{ \AA}$) of the quasar was obtained by [Morton et al. \(1980\)](#) and later on used by [Levshakov & Varshalovich \(1985\)](#) who reported the first ever detection of molecular-hydrogen absorption lines at high redshift. This was confirmed by [Foltz et al. \(1988\)](#) from $\Delta\lambda=1 \text{ \AA}$ spectroscopy and they derived $\log N(\text{H}_2) \sim 18$ (column densities will be expressed in cm^{-2} throughout). The first high-resolution Echelle spectrum ($R \sim 36\,000$) of Q 0528–250 was obtained by [Cowie & Songaila \(1995\)](#) using HIRES at Keck, and then and a number of other studies aiming to constrain the possible time variation of the proton-to-electron mass ratio from analysis of H_2 absorption lines ([Foltz et al. 1988](#); [Varshalovich & Potekhin 1995](#); [Potekhin et al. 1998](#); [Ubachs & Reinhold 2004](#); [King et al. 2008, 2011](#)).

[Ge et al. \(1997\)](#) used a MMT spectrum ($\Delta\lambda=2 \text{ \AA}$) of Q 0528–250 to study the physical conditions in the medium through modeling of the abundances of ionized species. They argued that the number density is about 20 cm^{-3} , the physical size of the components is $\sim 40 \text{ pc}$, and the distance of the absorber to the quasar is larger than 1 Mpc. However, most of the absorption lines measured in this spectrum are not resolved and are saturated, meaning that the column densities and hence the physical conditions of the gas may have been incorrectly derived. A high value of the number density in the H_2 -bearing gas, $n \sim 1000 \text{ cm}^{-3}$, was reported by [Srianand & Petitjean \(1998\)](#) from the analysis of a spectrum obtained using CASPEC at the 3.6 m telescope of La Silla observatory. To derive this number density, the latter authors used the observed relative populations of H_2 rotational levels up to $J = 4$. However, self-shielding was not taken into account and the H_2 column densities reported in this work are two orders of magnitude smaller than those derived at higher spectral resolution. The reported H_2 column densities indeed vary significantly between different analysis ($\log N(\text{H}_2) \sim 16.5$ in [Levshakov & Varshalovich 1985](#); [Ge et al. 1997](#); [Srianand & Petitjean 1998](#); [King et al. 2011](#) and $\log N(\text{H}_2) \sim 18$ in [Foltz et al. 1988](#); [Ledoux et al. 2003](#); [Klimenko et al. 2015](#)).

The high signal-to-noise, high-resolution spectrum obtained in 2002–2003 by [Ledoux et al. \(2003\)](#) using the UVES spectrograph mounted at the VLT made it possible to resolve two components in the H_2 absorption-line profiles, which favoured a high H_2 column-density value ([Srianand et al. 2005](#)). Using this spectrum, these authors also detected C I lines from the first-two fine-structure energy levels of the atom ground state, associated with one of the H_2 components. This allowed them to revise the number den-

¹ The exact value depends on the velocity range used to define PDLAs, possibly reaching an excess of an order of magnitude within 1000 km s^{-1} from the quasar systemic redshift.

sity and thermal pressure of the $\text{H}_2/\text{C I}$ -bearing gas to be $n_{\text{H}} \approx 25 - 270 \text{ cm}^{-3}$ and $P \approx 3250 - 17000 \text{ cm}^{-3}\text{K}$, respectively. [Ćirković et al. \(2006\)](#) used the same UVES spectrum to derive an upper limit on the column density of HD molecules, which resulted in loose constraints on the cosmic-ray ionizing flux. The detection of HD absorption in this system was reported by [King et al. \(2011\)](#), who measured $\log N(\text{HD}) = 13.27 \pm 0.07$ from new UVES observations carried out in 2009. The presence of C I, H_2 , and HD, suggests that the line-of-sight intercepts cold gas. Many observational campaigns aimed at detecting 21 cm absorption towards Q 0528–250 (e.g., [Carilli et al. 1996](#); [Curran et al. 2010](#); [Kanekar et al. 2014](#)), but they all led to lower limits on the ratio of the spin temperature to the covering fraction, $T_s/f > 700 \text{ K}$. Using these limits, [Srianand et al. \(2012\)](#) estimated the column density of HI associated with H_2 , $\log N(\text{HI}) \sim 20$, and constrained the size of the clouds to be $< 1.3 \text{ pc}$. Finally, [Klimenko et al. \(2015\)](#) used the combination of all available UVES observations to confirm the detection of HD and also noticed partial covering of the QSO-continuum emission region by the H_2 gas, with a covering fraction of $\sim 98\%$.

In addition to absorption-line studies, the field of the $z_{\text{abs}} = 2.811$ DLA towards Q 0528–250 was also searched for in emission. This is indeed one of the first DLAs where $\text{Ly}\alpha$ emission was detected. Using narrow-band imaging with EFOSC mounted at the ESO 3.6 m telescope, [Møller & Warren \(1993\)](#) detected three $\text{Ly}\alpha$ -emitting sources at $z_{\text{em}} \simeq 2.8$ with impact parameters of $\sim 1, 11,$ and 21 arcsec (corresponding to 8, 88, 168 kpc of transverse distance), from the quasar. [Warren & Møller \(1996\)](#) confirmed these findings and measured the redshifts, widths, and fluxes, of $\text{Ly}\alpha$ -emission lines from long-slit spectroscopy. Subsequent HST imaging and NTT/SUSI narrow-band imaging allowed to perform photometry and measure the sizes of the $\text{Ly}\alpha$ -emitting galaxies ([Møller et al. 1998](#)). The latter authors found that the source with the largest impact parameter is in fact made of two components and that its $\text{Ly}\alpha$ emission is much more extended than the continuum. This led them to argue that: (i) the $\text{Ly}\alpha$ -emitting sources correspond to a group of galaxies in the vicinity of the quasar; (ii) the $\text{Ly}\alpha$ emission of these sources is probably due to scattered emission from the quasar rather than in-situ star-formation; (iii) the source with the smallest impact parameter is most likely the DLA-galaxy counterpart. However, since radiative transfer of $\text{Ly}\alpha$ photons is complex, it is hard to constrain the physical separation between these galaxies and the quasar from $\text{Ly}\alpha$ emission.

3 SPECTROSCOPIC ANALYSIS

In the present study, we use the combination of all exposures obtained with the Ultraviolet and Visual Echelle Spectrograph (UVES; [Dekker et al. 2000](#)) on the Very Large Telescope during two epochs of observations, in 2001-2002, and in 2008-2009. The details of the observations and the data reduction are described in [Klimenko et al. \(2015\)](#).

We fit neutral atomic-hydrogen absorption lines using a one-component model (since the $\text{Ly}\alpha$ line is strongly damped) together with the unabsorbed quasar continuum modelled using six Chebyshev polynomials (for details on

Table 1. Fit results for C I ground-state and fine-structure lines originating from the first two excited levels of singly-ionized carbon. Total column densities, either across all components for a given fine-structure energy level, or summing up the contributions of all fine-structure levels in a given component, are provided.

Component	A	B	A + B
z	2.810973 ⁽⁺⁶⁾ ₍₋₆₎	2.8111231 ⁽⁺¹⁵⁾ ₍₋₁₂₎	
Δv^\dagger [km s ⁻¹]	-11.9 ^{+0.5} _{-0.5}	-0.1 ^{+0.1} _{-0.1}	
b [km s ⁻¹]	3.8 ^{+1.1} _{-1.1}	1.9 ^{+0.4} _{-0.4}	
$\log N(\text{C I})$	11.65 ^{+0.06} _{-0.09}	12.06 ^{+0.02} _{-0.02}	12.20 ^{+0.02} _{-0.02}
$\log N(\text{C I}^*)$	11.83 ^{+0.07} _{-0.07}	12.27 ^{+0.02} _{-0.03}	12.40 ^{+0.02} _{-0.02}
$\log N(\text{C I}^{**})$	< 11.34	11.95 ^{+0.03} _{-0.03}	11.99 ^{+0.04} _{-0.04}
$\log N_{\text{tot}}$	12.07 ^{+0.07} _{-0.06}	12.59 ^{+0.02} _{-0.01}	12.71 ^{+0.02} _{-0.02}

[†] Velocity offset relative to $z = 2.811124$.

Table 2. Fit results for Si II* lines, originating from the first excited level of singly-ionized silicon.

Component	A	B
z	2.810973	2.811129(3)
Δv^\dagger [km s ⁻¹]	-11.9	0.4 ^{+0.2} _{-0.2}
b [km s ⁻¹]	3.8 [‡]	3.5 ^{+0.5} _{-0.6}
$\log N(\text{Si II}^*)$	< 11	11.37 ^{+0.03} _{-0.03}

[†] Velocity offset relative to $z = 2.811124$.

[‡] In this component, the redshift and Doppler parameter are taken from the fit of the C I lines, and were fixed to these values when fitting Si II* to determine an upper limit on its column density.

the technique, see, e.g., [Balashev et al. 2019](#)). We find that the total neutral-hydrogen column density is $\log N(\text{HI}) = 21.37 \pm 0.01$ centered on $z_{\text{abs}} = 2.811379(20)$ in agreement with the value reported by [Ledoux et al. \(2006\)](#) ($\log N(\text{HI}) = 21.35 \pm 0.07$). The $\text{Ly}\alpha$ absorption line is redshifted by $\sim 2000 \text{ km s}^{-1}$ compared to the reconstructed profile of the $\text{Ly}\alpha$ emission line. However, it is known that $\text{Ly}\alpha$ emission may be blue-shifted relative to the systemic redshift of the QSO. We therefore consider our estimate with caution, but note that previous work indicating a systemic redshift of $z_{\text{em}} = 2.7783 \pm 0.007$ ([Ellison et al. 2010](#)) would lead to an even larger velocity ($\sim 3500 \text{ km s}^{-1}$).

The observed metal-line profiles are complex, exhibiting at least ~ 20 individual velocity components with two main clumps at $z_{\text{abs}} \approx 2.8114$ and 2.8138 , respectively. Molecular hydrogen is detected within two components of the bluest clump only, at $z_{\text{abs}} = 2.810995(2)$ and $2.811124(2)$, with total column densities of $\log N(\text{H}_2) = 18.10 \pm 0.02$ and 17.82 ± 0.02 , respectively ([Klimenko et al. 2015](#)). We adopt these values in the following analysis as they were derived from the same spectrum. Deuterated molecular hydrogen (HD) is detected in lines originating from the $J = 0$ rotational level corresponding to the H_2 component at $z_{\text{abs}} = 2.811124$. The total HD column density is $\log N = 13.33 \pm 0.02$ ([Klimenko et al. 2015](#)). Throughout the paper, we use $z = 2.811124$ to define the zero of the velocity scale.

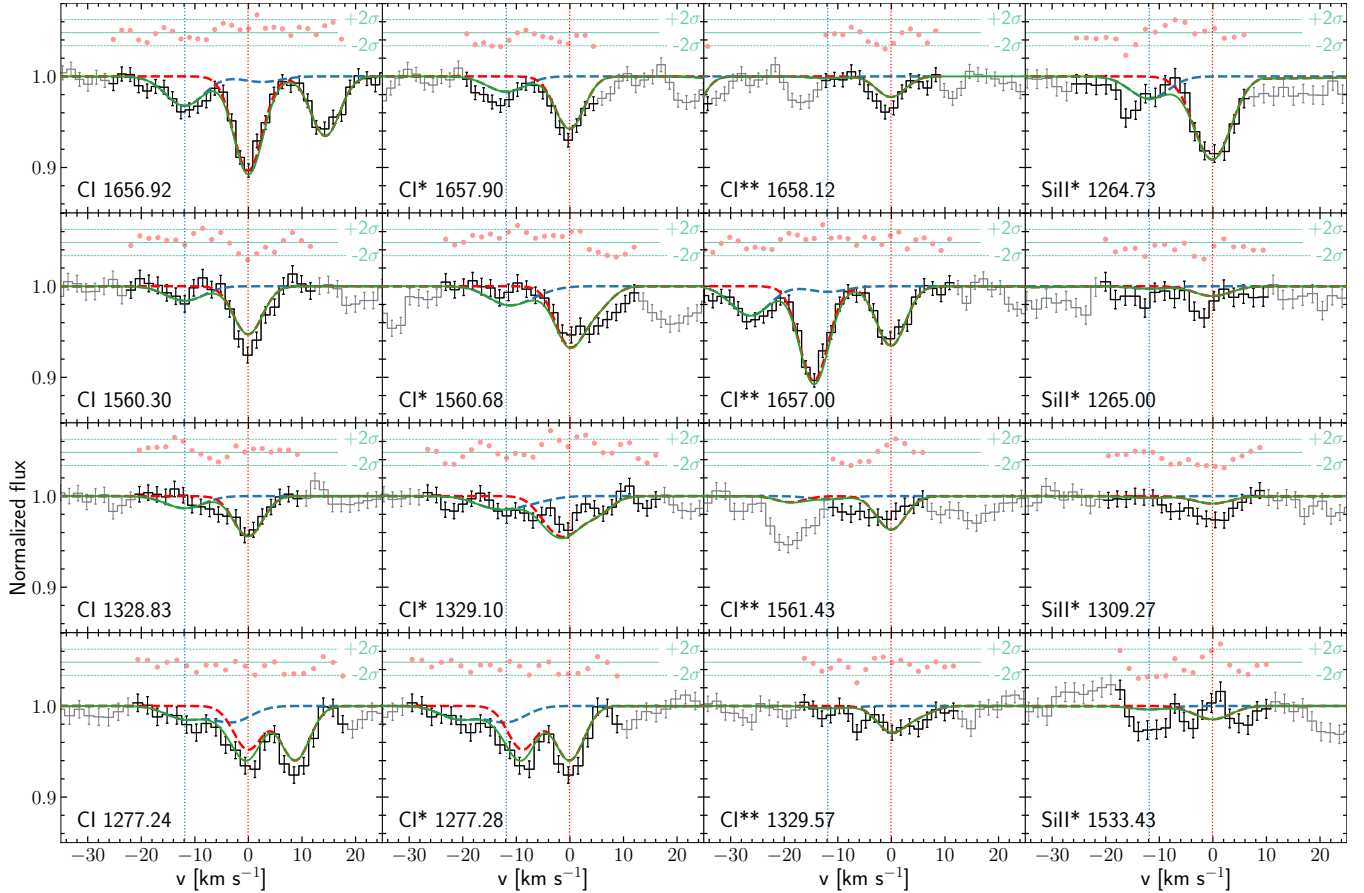


Figure 1. Voigt-profile fits to C I and Si II lines at $z_{\text{abs}} = 2.811$ towards Q 0528–250. The observed spectrum is shown in grey except for those pixels used to constrain the model which are displayed in black. The blue and red dashed curves are the fits of components A and B, respectively, and their joint contribution is shown by green solid line. Fit residuals are displayed in each panel above the spectra. The zero-velocity of the x-axis corresponds to a redshift of $z = 2.811124$.

3.1 C I fine-structure levels

Absorption lines corresponding to transitions from the three fine-structure energy levels of the C I ground state are detected in two components that coincide in velocity with the detected H₂ components. In the following, we will refer to the component near the zero-velocity redshift as B (or red) and the component bluewards of it as A (or blue). We use the transitions around 1656, 1560, 1328, and 1277 Å, to measure the column densities in all three C I fine-structure levels using a two-component model with tied Doppler parameters. This implicitly assumes that the medium associated with each component is homogeneous. The fitted C I-line profiles are shown in Fig. 1 and the fit parameters are given in Table 1. The Doppler parameter derived for the blue component is consistent with that obtained from H₂ (see Klimenko et al. 2015). However, we find higher Doppler parameter for the red C I component than in lower H₂ rotational levels. Notwithstanding, we note that C I lines are weak so the derived column densities (and especially their ratios) are not very sensitive to the exact value of the Doppler parameter. The column densities derived in both components indicate a relatively high C I excitation compared to what is usually seen in intervening high- z DLAs: $J = 1$ is in the present case

more populated than $J = 0$, when the opposite is normally seen (see, e.g., Jorgenson et al. 2010; Balashev et al. 2011; Noterdaeme et al. 2017). The observed column-density ratios is used in Sect. 4 to estimate the hydrogen number density of the absorbing medium.

3.2 Si II fine-structure levels

We detect ionized silicon in its first excited state (Si II^{*}) from its strong absorption line at rest-frame wavelength 1264 Å. This absorption is confidently detected in the component coinciding with the red component of the H₂- and C I-line profiles, while some absorption can only be hinted at the position of the strongest metal lines. The fitted Si II^{*} line is shown in the right-most panels of Fig. 1 and the corresponding fit parameters are given in Table 2. For component B, we place an upper limit on the column density assuming the redshift and Doppler parameter obtained from C I.

It is not possible to accurately determine the Si II column density associated with the H₂-detected components of the DLA since the only Si II absorption line which is not completely saturated (i.e., Si II λ 1808) is blended with telluric absorption. Additionally, many velocity components in the intermediate-saturation regime of the Si II λ 1808 line are

blended with each other, which increases the degeneracy to the fitting solution as derived from a single line. Therefore, we roughly estimate the Si II column density corresponding to the H₂-detected component using the measured Zn II column densities. For this, we fit Zn II, Cr II, Ni II, and Fe II lines assuming the same redshift and Doppler parameter for each metal species within a given component. We provide the fit results in Table A1 of the Appendix and show the fits in Figs. A1 and A2. We measure Zn II column densities of $\log N = 11.99^{+0.05}_{-0.04}$ and $12.28^{+0.01}_{-0.02}$ in the components closest to the blue and red H₂-detected components, respectively. The total Zn II column density is $\log N = 13.25^{+0.02}_{-0.02}$, yielding an average DLA metallicity (calculated using solar abundances from Asplund et al. 2009) based on Zn II of $[X/H] = -0.68^{+0.02}_{-0.02}$. This metallicity is ~ 0.2 dex larger than that derived by De Cia et al. (2016) due to our more sophisticated decomposition of this complex line profile. We find that the depletion of Cr, Ni, and Fe relative to Zn is $-0.47^{+0.01}_{-0.01}$, $-0.57^{+0.01}_{-0.01}$, and $-0.76^{+0.01}_{-0.01}$, respectively, based on total column densities (which is also similar on a component-by-component basis). This suggests that the depletion of Si relative to Zn is ~ 0.1 with a dispersion of around 0.15 (De Cia et al. 2016). Therefore, we estimate column densities of $\log N(\text{Si II}) = 14.84^{+0.15}_{-0.15}$ and $15.13^{+0.15}_{-0.15}$, in the blue and red H₂-detected components, respectively.

4 PHYSICAL CONDITIONS

We use the observed excitation of the fine-structure energy levels of the C I and Si II ground states to constrain the physical conditions in the cold-gas phase probed by the H₂/C I-detected components of the DLA. For this, we perform standard calculations alike POPRATIO (Silva & Viegas 2001), the details of which, and information on the data we use, is given in Balashev et al. (2017). Our calculations assume a homogeneous medium where C I and Si II fine-structure levels are populated by collisions with atomic and molecular hydrogen², and pumping by UV photons³. The cosmic microwave background radiation intensity is fixed by the redshift of the DLA. The observed molecular fraction yields the fraction of H I/H₂ – two main collisional partners. We assume that hydrogen is predominantly in atomic form since the H₂ column density is too low for H₂ to be completely self-shielded. PDR Meudon code calculations for the derived physical conditions strongly support this assumption. We are hence left with three parameters which altogether characterize the excitation of C I and Si II: the hydrogen number density⁴, n_{H} , the UV radiation-field strength, and the

² We also take into account Helium which, however, only has a minor contribution to the excitation. On the other hand, we neglect collisions with electrons due to the low-ionization fraction of the Cold Neutral Medium associated with the H₂/C I components.

³ Si II and C I fine-structure levels can be populated by direct radiative excitation. This kind of excitation requires very strong IR/sub-mm fields. Principally, such photons can be supplied by AGN. However, we checked that for a typical broad-band AGN spectrum, UV pumping dominates over direct excitation by several orders of magnitude both for Si II and C I.

⁴ In our case, since we consider a neutral medium with low molecular fraction, hydrogen is mostly in atomic form and therefore $n_{\text{H}} = n_{\text{H I}} + n_{\text{H}_2} + 2n_{\text{H}_2} \approx n_{\text{H I}}$.

temperature, T . In contrast to C I whose lines are optically thin, the Si II lines corresponding to the strongest transitions that participate in UV pumping are optically thick. We take into account the reduction of UV pumping for Si II using the estimated column densities in components A and B (see Sect. 3.2). We build a grid of values for each of these parameters, within reasonable ranges, and compare calculated relative populations with the observed ones, assuming Gaussian probability distributions for the measurement uncertainties.

To simplify the representation of the results, we perform calculations separately onto two 2D planes of parameter space, $n_{\text{H}} - T$, and $n_{\text{H}} - \text{UV}$, respectively. This is justified since the kinetic temperature is well constrained from T_{01} , which is the excitation temperature estimated from the relative populations of the H₂ $J = 1/J = 0$ rotational levels, which was previously found to be $T_{01} = 141 \pm 6$ K and 167 ± 13 K in components A and B, respectively (Klimenko et al. 2015). Additionally, we found that pumping by UV photons has a minor effect on the populations of C I fine-structure levels.

In Fig. 2, we show the constraints on number density and temperature inferred from C I, Si II, HD, and T_{01} , whilst neglecting UV pumping, in components A and B individually. In component B at $T \sim T_{01}$ the estimate based on Si II provides higher number density than C I does. As shown below, this is due to the fact that for Si II UV pumping cannot be neglected. Joint estimates from both species assuming $T_{\text{kin}} = T_{01}$ are shown as red contours in Fig. 2, yielding number densities of 240^{+70}_{-60} and 310^{+40}_{-30} cm⁻³ in the blue and red components, respectively. HD molecules in the $J = 0$ rotational level were previously detected in the red component with column density $\log N = 13.33 \pm 0.02$ (Klimenko et al. 2015). Here, we derive in this particular component an upper limit on the column density of HD in the $J = 1$ rotational level of $\log N < 12.90$. In typical conditions of the cold ISM, the HD $J = 1$ rotational level is mainly populated by collisions (Balashev et al. 2010). The constraint, in the temperature-density plane, resulting from the upper limit on the relative populations of the HD $J = 1/J = 0$ rotational levels, using the same code as above, is shown (by a purple line) in Fig. 2 (right panel). It is consistent with previous estimates from both C I and Si II.

We present in Fig. 3 the constraints on number density and UV flux in components A and B based on the excitation of C I and Si II assuming $T_{\text{kin}} = T_{01}$ in our calculations. We also use the measured excitation of high H₂ rotational levels (taken from Klimenko et al. 2015) to further restrain the solutions (see Balashev et al. 2019). Indeed, H₂ rotational levels are populated by collisions and radiative pumping in resonant lines in a UV wavelength range similar to C I and Si II. However, resonant lines quickly saturate when external UV radiation penetrates the cloud and therefore the excitation of H₂ rotational levels strongly depends upon the radiative transfer of resonant UV lines in the H₂ Lyman and Werner bands, in which case one cannot assume homogeneity. We hence use in this case the PDR Meudon code (Le Petit et al. 2006) that calculates the full radiative transfer in H₂ lines to compare modeled excitation of H₂ rotational levels with the observations. We use pseudo-spherical models of constant density, and metallicity and dust content of one tenth of solar. As for C I and Si II, we end up with two

external parameters: the hydrogen number density, n_{H} , and the strength of the UV radiation field. We run a grid of models with 10 points evenly spaced logarithmically for both the number density and the UV field, varied within the following ranges: $\log n_{\text{H}} = 1.4$ and $\log \text{UV} = -0.5..3$ (where UV is expressed in units of the Draine’s field), respectively. When comparing model results with the observations, we take into account the column densities measured in all detected H_2 rotational levels up to $J = 5$. We also use the column densities of H_2 rotational levels calculated at a depth in the cloud corresponding to half of the total observed H_2 column density. This essentially simulates the result of a cloud illuminated on both sides, with a total H_2 column density equal to the measured one. We include a factor of 2 (0.3 dex) uncertainty on the observed H_2 column densities to take into account geometric effects since the H_2 cloud is most likely not exactly spherical. We smooth the results of our calculations by interpolating the H_2 excitation diagram on a denser grid in the $\log n_{\text{H}}\text{-log UV}$ parameter space, and compare this to the observed H_2 population in Fig. 3. We find that the H_2 , C I, and Si II 2D-probability density functions individually cover a large area of the parameter space but have different shapes and intersect in a localised region. Joint estimates (shown in the figure by red contours) provide the following constraints on the number density and UV field strength: $n_{\text{H}} = 190^{+70}_{-50} \text{ cm}^{-3}$ (resp. $260^{+30}_{-20} \text{ cm}^{-3}$) and $\text{UV} = 10^{+5}_{-3}$ (resp. 14^{+3}_{-3}) in component A (resp. component B). We note that at given joint constraints C I is predominantly populated by collision, while Si II is excited by UV pumping and collisions.

5 DISCUSSION

In Figs. 2 and 3, we give estimates of number density, temperature, and UV flux in a sample of $\text{H}_2/\text{C I}$ -bearing DLAs, which we also determined using our code from the excitation of C I fine-structure and H_2 rotational levels (i.e., the compilation of data from Balashev et al. 2019). One can see that the UV flux in both components of the DLA towards Q 0528–250, as well as the thermal pressure (shown by inclined dashed lines in the figure), are higher than the average of other H_2 -bearing DLAs. Balashev et al. (2017, 2019) also reported tentative evidence of an increase of thermal pressure with increasing hydrogen column density. This suggests that high H I column-density systems have smaller impact parameters than typical DLAs and hence probe the inner regions of galaxies where the thermal pressure may be enhanced by high UV flux.⁵ However, the DLA studied here has significantly higher thermal pressure than suggested by this trend for $\log N(\text{H I}) \sim 21.35$. We suggest that the relatively high pressures and high UV fluxes observed in this DLA are instead due to its proximity to the quasar.

⁵ This is in line with the findings of Noterdaeme et al. (2014) and Ranjan et al. (2019) based on, respectively, statistical and direct detection of star-formation signatures (which correlate with UV flux) at no more than a few projected kpc from extremely strong DLAs ($\log N(\text{H I}) \sim 22$).

5.1 Origin of the DLA gas

From a constrained UV flux of about 10–15 times the Draine’s field and the known quasar luminosity, we can estimate the distance between the H_2 -detected components of the DLA and the AGN assuming the quasar dominates the incident UV flux. Corrections due to dust reddening are negligible since the DLA has a low metallicity and we do not see reddening in the quasar spectrum. Under these circumstances, we infer a distance of $\sim 150\text{--}200$ kpc. This distance suggests that the DLA is located with a group of galaxies rather than being produced by the quasar-host galaxy itself. However, such a distance does not exclude the possibility that the DLA gas is compressed by the mechanical output of the AGN. Indeed, Q 0528–250 is a blazar, i.e., the line-of-sight where the absorption system is seen coincides with the direction of the jet, which can have an extension comparable to the distance we derive (see, e.g., Blandford et al. 2019). However, the redshift of the DLA is higher than that of the quasar which implies that the DLA is moving towards the quasar and cannot be outflowing material.

As mentioned in Sect. 2, emission-line searches have revealed three Ly α emitters around Q 0528–250 that span ~ 100 kpc in the transverse direction. One object is located at an impact parameter of ~ 8 kpc from the quasar (Warren & Møller 1996) while the object at the largest impact parameter was resolved into two sources from HST imaging (Møller et al. 1998). The Ly α emission-line profiles are broad and it is difficult to firmly establish the association of any of those with the DLA. However, the most reasonable assumption is that the DLA absorption is associated with the object at the lowest impact parameter, which is corroborated by many lines of evidence (e.g., Krogager et al. 2017, and references therein). Since we have estimated the distance between the DLA and the QSO to be $\lesssim 200$ kpc, which is similar to the transverse separation between the detected Ly α emission sources, these sources probably form a group of which the QSO-host galaxy is a major member.

Additionally, low-ionization metal lines associated with the DLA exhibit complex kinematics with two prominent velocity clumps separated by $\sim 200 \text{ km s}^{-1}$. This may suggest that the overall absorption originates from two compact galaxies and/or includes tidally-stripped gas due to galaxy interaction (see, e.g., Kacprzak et al. 2010). We cannot disentangle between these possibilities as we measured the physical conditions and constrained the distance of the gas from the $\text{H}_2/\text{C I}$ components of the bluer clump only. However, this is in line with previous findings (e.g., Ledoux et al. 2006; Christensen et al. 2014) where the correlation between gas velocity dispersion and metallicity in DLAs has been interpreted as a result of increasingly more massive and complex environments. This is also supported by recent ALMA observations of J 1201+2117 from which extreme DLA kinematics has been proposed as the signpost of major mergers in normal galaxies at high redshift (Prochaska et al. 2019).

5.2 Physical extent of H_2 -bearing clouds and partial covering

Using derived number densities, we can estimate the physical extent of the clouds along the line-of-sight. From PDR mod-

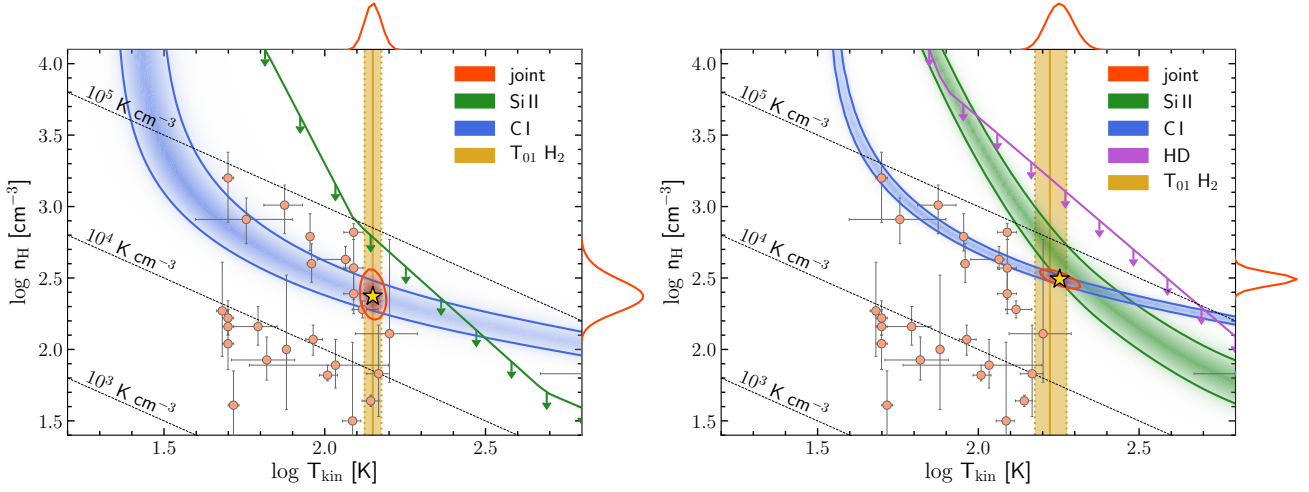


Figure 2. Estimates of hydrogen number density and temperature in component *A* (left panel) and *B* (right panel) of the DLA, associated with the $\text{H}_2/\text{C I}$ -bearing gas. The green, blue, violet, and yellow colors are used to show the constraints from Si II, C I, HD, and T_{01} (i.e., the H_2 ortho-to-para ratio), respectively. Color gradients depict the derived probability-density functions, with contour lines encompassing 68.3% of them. The red contour in each panel is the joint constraint, with a yellow star marking the location of the most likely value. The red curves on the top and right-hand side axes show the marginalized distributions arising from the joint fit of T_{kin} and n_{H} , respectively. Light red circles are estimates of n_{H} and T_{01} in generic $\text{H}_2/\text{C I}$ -bearing DLAs at high redshift (Balashev et al. 2019).

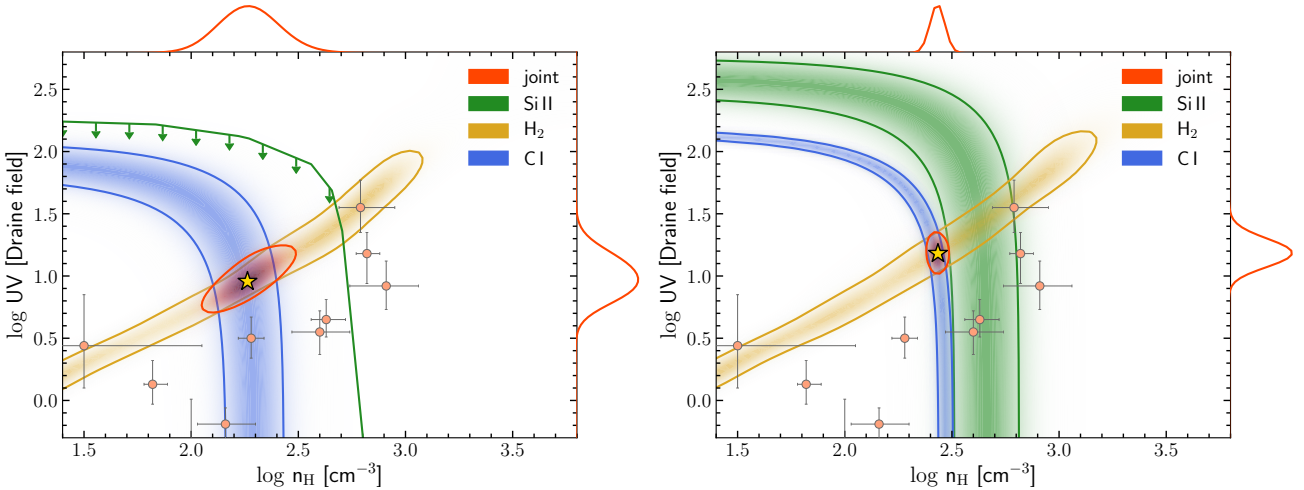


Figure 3. Estimates of hydrogen number density and UV flux in component *A* (left panel) and *B* (right panel) of the DLA, associated with the $\text{H}_2/\text{C I}$ -bearing gas, using constraints from Si II, C I, and H_2 . Drawing conventions are the same as in Fig. 2. The constraints arising from the excitation of H_2 rotational levels are displayed in yellow.

eling, we found that H I is the dominant species within the $\text{H}_2/\text{C I}$ -detected components. However, one cannot directly measure how much H I is associated with each H_2 component since individual H I lines are unresolved. This can however be estimated indirectly. Firstly, we derived a column density $\log N \sim 20$ using the Meudon PDR code using the measured H_2 column densities as input, a UV flux ~ 15 times stronger than Draine’s field, and a number density $n_{\text{H}} \sim 300 \text{ cm}^{-3}$ (our derived best-fit parameters). Secondly, the Zn II column density associated with the H_2 components is about 1.2 order of magnitude smaller than the overall zinc column density. Assuming the metallicity is the same in each component of the DLA, we estimate the H I column density associated with the H_2 components to be $\log N \sim 20.1$. Srianand et al. (2012) estimated a similar H I column density in the

cold phase of the ISM (i.e., $\log N \sim 20$) based on an upper limit on T_s/f from non-detection of H I 21-cm absorption.

The most conservative estimate of the total column density of particles (atomic and molecular hydrogen altogether) associated with the two H_2 components of the DLA ranges between $\log N \sim 21.30$ and ~ 18.0 . Using these values, the upper and lower bounds on the physical extent of the clouds are $< 0.1 \text{ pc}$ and $> 100 \text{ a.u.}$, respectively. Assuming a value of $\log N \sim 20$ (see above), we infer a typical size for the clouds of $\sim 10^4 \text{ a.u.}$

The small physical extent of the cloud and/or the jet orientation provide natural explanations for the $\sim 2\%$ line-flux residual seen in the core of the saturated H_2 lines (Klimenko et al. 2015). Indeed, this suggests the continuum source of the quasar is not fully covered by the H_2 -bearing clouds. Partial covering can be explained either by (i) comparable

sizes of the accretion disc and the H₂ absorbing medium; (ii) jet-induced scintillation in a clumpy medium; (iii) emission from the quasar- and/or the DLA-absorbing galaxy (Cai et al. 2014).

Studying the possible variation with time of the residual flux may provide clues to discriminate between these scenarios since each of them occur on different timescales. In the first scenario (geometric effects), flux variations are expected due to the relative projected motion of the absorber, quasar-emitting region, and observer (Boissé et al. 2015). The velocity of this motion can be estimated as $\sim 2000 \text{ km s}^{-1}$ in the case of the DLA towards Q 0528–250 based on the velocity difference between QSO and DLA projected on the line-of-sight. This corresponds to a transverse shift of $\sim 400 \text{ a.u.}$ in a year. Over 25 years (the available time span of available observations), this is comparable to the size of the absorber assuming the transverse size of the H₂ system is the same as that derived longitudinally. Under the second scenario (jet scintillation), the timescale and magnitude of the expected variation of flux residuals correspond to the quasar variability itself since observed residuals are scattered emission. However, since the exact position of the scintillated cloud is unknown, the timelag between quasar continuum and scintillated emission is uncertain making quantitative conclusions from this observation complicated. Under the third scenario, variability of residual flux is not expected over timescales smaller than a few decades.

6 CONCLUSIONS

We presented the detection of excited fine-structure energy levels of singly ionized silicon and neutral carbon associated with the $z_{\text{abs}} = 2.811$ PDLA towards Q 0528–250. We measured total Si II* and C I column densities of 11.37 ± 0.03 and 12.71 ± 0.02 , respectively. The metallicity of the DLA is $\log Z/Z_{\odot} = -0.68 \pm 0.02$ based on [Zn II/H I]. From the relative populations of the fine-structure levels of Si II and C I, as well as the populations of H₂ rotational levels, we were able to constrain the hydrogen number density and UV flux in the cold neutral phase of this DLA. We found number densities $n_{\text{H}} = 190^{+70}_{-50} \text{ cm}^{-3}$ and $260^{+30}_{-20} \text{ cm}^{-3}$ in the blue and red velocity components, respectively, where both C I and H₂ are detected. The strengths of the UV field in Draine’s unit were derived to be $I_{\text{UV}} = 10^{+5}_{-3}$ and 14^{+3}_{-3} in each of the two components, respectively. The high thermal pressure in comparison with intervening DLAs and the enhanced UV flux measured in this particular DLA are most likely due to the proximity of the quasar. Assuming the UV flux is dominated by the quasar, we estimated the distance between the quasar and the absorbing gas to be $\sim 150 - 200 \text{ kpc}$, and its physical extent $\sim 10^4 \text{ a.u.}$ This favours a scenario where the absorption occurs in a companion galaxy located in the group where the quasar-host galaxy resides. This is in line with studies in emission that revealed the presence of several galaxies around the quasar.

7 DATA AVAILABILITY

The paper is based on the data that is available on the archive of European Southern Observatory archive under

ESO programs 66.A-0594, 68.A-0600, 68.A-0106, and 082.A-0087.

ACKNOWLEDGEMENTS

We thank the referee for useful comments and suggestions. This research was partially supported by RFBR grant 18-52-15021. SB is supported by the Foundation for the Advancement of Theoretical Physics and Mathematics “BASIS” and is grateful to the European Southern Observatory in Chile for hospitality as visiting scientist. We acknowledge support from the French *Agence Nationale de la Recherche* under ANR grant 17-CE31-0011-01, project “HIH2” (PI: Noterdaeme).

REFERENCES

- Asplund M., Grevesse N., Sauval A. J., Scott P., 2009, *ARA&A*, **47**, 481
- Balashev S. A., Ivanchik A. V., Varshalovich D. A., 2010, *Astronomy Letters*, **36**, 761
- Balashev S. A., Petitjean P., Ivanchik A. V., Ledoux C., Srianand R., Noterdaeme P., Varshalovich D. A., 2011, *MNRAS*, **418**, 357
- Balashev S. A., et al., 2017, *MNRAS*, **470**, 2890
- Balashev S. A., et al., 2019, *MNRAS*, **490**, 2668
- Blandford R., Meier D., Readhead A., 2019, *ARA&A*, **57**, 467
- Boissé P., Bergeron J., Prochaska J. X., Péroux C., York D. G., 2015, *A&A*, **581**, A109
- Cai Z., et al., 2014, *ApJ*, **793**, 139
- Carilli C. L., Lane W., de Bruyn A. G., Braun R., Miley G. K., 1996, *AJ*, **111**, 1830
- Christensen L., Møller P., Fynbo J. P. U., Zafar T., 2014, *MNRAS*, **445**, 225
- Ćirković M. M., Damjanov I., Lalović A., 2006, *Baltic Astronomy*, **15**, 571
- Cowie L. L., Songaila A., 1995, *ApJ*, **453**, 596
- Curran S. J., Tzanavaris P., Darling J. K., Whiting M. T., Webb J. K., Bignell C., Athreya R., Murphy M. T., 2010, *MNRAS*, **402**, 35
- De Cia A., Ledoux C., Mattsson L., Petitjean P., Srianand R., Gagnaud I., Jenkins E. B., 2016, *A&A*, **596**, A97
- Dekker H., D’Odorico S., Kaufer A., Delabre B., Kotzłowski H., 2000, in Iye M., Moorwood A. F., eds, *Society of Photo-Optical Instrumentation Engineers (SPIE) Conference Series Vol. 4008*, Proc. SPIE. pp 534–545, doi:10.1117/12.395512
- Ellison S. L., Yan L., Hook I. M., Pettini M., Wall J. V., Shaver P., 2002, *A&A*, **383**, 91
- Ellison S. L., Prochaska J. X., Hennawi J., Lopez S., Usher C., Wolfe A. M., Russell D. M., Benn C. R., 2010, *MNRAS*, **406**, 1435
- Fathivavsari H., Petitjean P., Zou S., Noterdaeme P., Ledoux C., Krühler T., Srianand R., 2017, *MNRAS*, **466**, L58
- Fathivavsari H., et al., 2018, *MNRAS*, **477**, 5625
- Finley H., et al., 2013, *A&A*, **558**, A111
- Foltz C. B., Chaffee Frederic H. J., Black J. H., 1988, *ApJ*, **324**, 267
- Ge J., Bechtold J., Walker C., Black J. H., 1997, *ApJ*, **486**, 727
- Hennawi J. F., Prochaska J. X., Kollmeier J., Zheng Z., 2009, *ApJ*, **693**, L49
- Jauncey D. L., Wright A. E., Peterson B. A., Condon J. J., 1978, *ApJ*, **221**, L109
- Jiang P., et al., 2016, *ApJ*, **821**, 1
- Jorgenson R. A., Wolfe A. M., Prochaska J. X., 2010, *ApJ*, **722**, 460

- Kacprzak G. G., Murphy M. T., Churchill C. W., 2010, *MNRAS*, **406**, 445
- Kanekar N., et al., 2014, *MNRAS*, **438**, 2131
- King J. A., Webb J. K., Murphy M. T., Carswell R. F., 2008, *Phys. Rev. Lett.*, **101**, 251304
- King J. A., Murphy M. T., Ubachs W., Webb J. K., 2011, *MNRAS*, **417**, 3010
- Klimenko V. V., Balashev S. A., Ivanchik A. V., Ledoux C., Noterdaeme P., Petitjean P., Srianand R., Varshalovich D. A., 2015, *MNRAS*, **448**, 280
- Krogager J. K., Møller P., Fynbo J. P. U., Noterdaeme P., 2017, *MNRAS*, **469**, 2959
- Le Petit F., Nehmé C., Le Bourlot J., Roueff E., 2006, *The Astrophysical Journal Supplement Series*, **164**, 506
- Ledoux C., Petitjean P., Srianand R., 2003, *MNRAS*, **346**, 209
- Ledoux C., Petitjean P., Fynbo J. P. U., Møller P., Srianand R., 2006, *A&A*, **457**, 71
- Levshakov S. A., Varshalovich D. A., 1985, *MNRAS*, **212**, 517
- Møller P., Warren S. J., 1993, *A&A*, **270**, 43
- Møller P., Warren S. J., Fynbo J. U., 1998, *A&A*, **330**, 19
- Morton D. C., Jian-Sheng C., Wright A. E., Peterson B. A., Jauncey D. L., 1980, *MNRAS*, **193**, 399
- Noterdaeme P., Petitjean P., Pâris I., Cai Z., Finley H., Ge J., Pieri M. M., York D. G., 2014, *A&A*, **566**, A24
- Noterdaeme P., et al., 2017, *A&A*, **597**, A82
- Noterdaeme P., Balashev S., Krogager J. K., Srianand R., Fathivavsari H., Petitjean P., Ledoux C., 2019, *A&A*, **627**, A32
- Potekhin A. Y., Ivanchik A. V., Varshalovich D. A., Lanzetta K. M., Baldwin J. A., Williger G. M., Carswell R. F., 1998, *ApJ*, **505**, 523
- Prochaska J. X., Hennawi J. F., Herbert-Fort S., 2008, *ApJ*, **675**, 1002
- Prochaska J. X., Neeleman M., Kanekar N., Rafelski M., 2019, *ApJ*, **886**, L35
- Ranjan A., Noterdaeme P., Krogager J. K., Petitjean P., Srianand R., Balashev S. A., Gupta N., Ledoux C., 2019, *A&A*, **633**, A125
- Silva A. I., Viegas S. M., 2001, *Computer Physics Communications*, **136**, 319
- Smith H. E., Jura M., Margon B., 1979, *ApJ*, **228**, 369
- Srianand R., Petitjean P., 1998, *A&A*, **335**, 33
- Srianand R., Petitjean P., Ledoux C., Ferland G., Shaw G., 2005, *MNRAS*, **362**, 549
- Srianand R., Gupta N., Petitjean P., Noterdaeme P., Ledoux C., Salter C. J., Saikia D. J., 2012, *MNRAS*, **421**, 651
- Ubachs W., Reinhold E., 2004, *Phys. Rev. Lett.*, **92**, 101302
- Varshalovich D. A., Potekhin A. Y., 1995, *Space Sci. Rev.*, **74**, 259
- Warren S. J., Møller P., 1996, *A&A*, **311**, 25

APPENDIX A: METAL-LINE FITS

In Table A1, we present the complete results from fitting metal lines in the DLA at $z_{\text{abs}} = 2.811$ towards Q 0528–250 using multi-component Voigt profiles and sampling through the MCMC technique. The observed and synthetic profiles of Zn II, Cr II, Ni II, and Fe II are shown in Figs. A1 and A2.

This paper has been typeset from a $\text{T}_{\text{E}}\text{X}/\text{L}^{\text{A}}\text{T}_{\text{E}}\text{X}$ file prepared by the author.

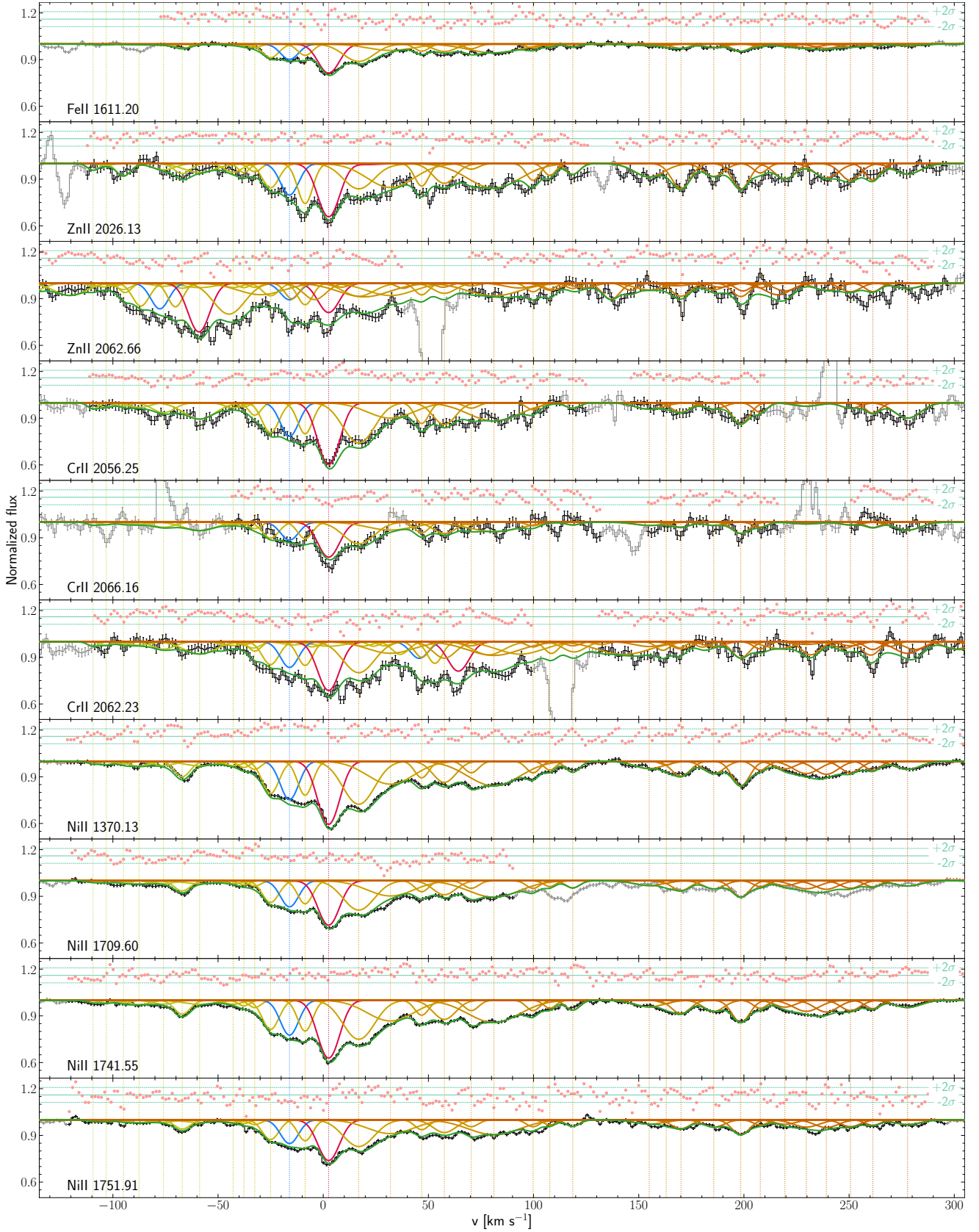


Figure A1. Voigt-profile fits to Zn II, Cr II, Ni II, and Fe II lines at $z_{\text{abs}} = 2.811$ towards Q0528–250. The observed spectrum is shown in grey except for those pixels used to constrain the model which are instead displayed in black. The total fit profile is represented by the green curve. Components *A* and *B* are displayed in blue and red, respectively, and the other sub-components are shown in yellow and orange. Fit residuals are displayed in each panel above the spectra. The zero-velocity of the x-axis corresponds to a redshift of $z = 2.811124$.

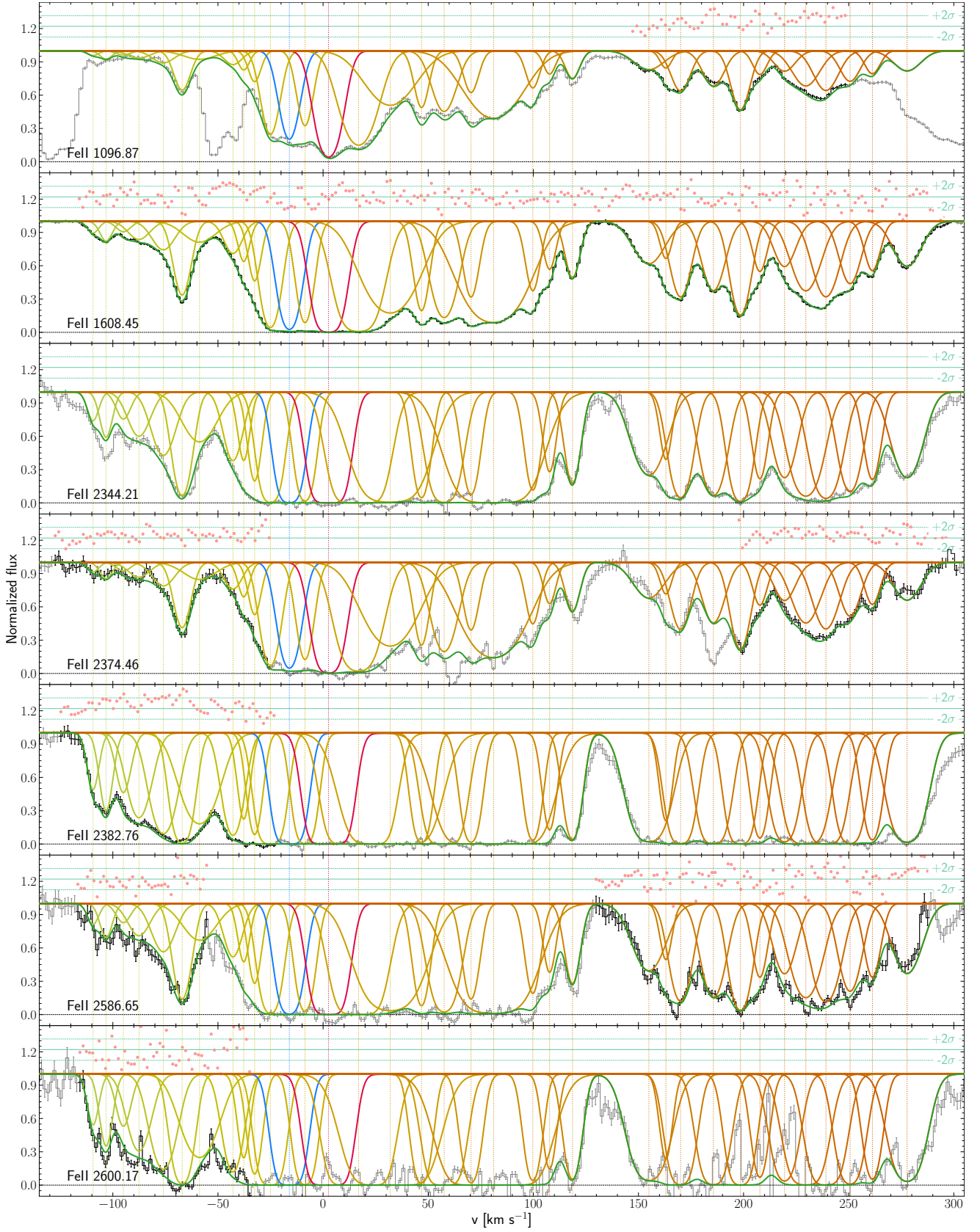


Figure A2. Continuation of Fig. A1.

Table A1. Result of Voigt-profile fitting to metal lines in the DLA at $z_{\text{abs}} = 2.811$ towards Q 0528–250.

Comp.	z	Δv^\dagger [km s $^{-1}$]	b [km s $^{-1}$]	$\log N(\text{Zn II})$	$\log N(\text{Cr II})$	$\log N(\text{Fe II})$	$\log N(\text{Ni II})$
1	2.8097329 ⁽⁺²²⁾ ₋₂₂	-109.5	1.8 ^{+0.3} _{-0.2}	11.03 ^{+0.10} _{-0.21}	11.67 ^{+0.15} _{-0.21}	12.49 ^{+0.03} _{-0.02}	11.72 ^{+0.03} _{-0.08}
2	2.8098120 ⁽⁺²⁴⁾ ₋₁₇	-103.3	2.3 ^{+0.2} _{-0.2}	< 10.8	11.59 ^{+0.14} _{-0.22}	12.77 ^{+0.02} _{-0.02}	11.84 ^{+0.04} _{-0.06}
3	2.809917 ⁽⁺³⁾ ₋₃	-95.0	3.4 ^{+0.6} _{-0.5}	11.42 ^{+0.04} _{-0.10}	11.52 ^{+0.14} _{-0.32}	12.53 ^{+0.07} _{-0.09}	11.83 ^{+0.08} _{-0.10}
4	2.810011 ⁽⁺⁶⁾ ₋₄	-87.6	6.2 ^{+0.6} _{-0.6}	< 10.5	11.84 ^{+0.13} _{-0.23}	12.95 ^{+0.05} _{-0.04}	12.24 ^{+0.03} _{-0.06}
5	2.810158 ⁽⁺³⁾ ₋₄	-76.0	6.5 ^{+0.2} _{-0.2}	11.29 ^{+0.04} _{-0.06}	12.19 ^{+0.06} _{-0.07}	13.19 ^{+0.01} _{-0.01}	12.21 ^{+0.02} _{-0.05}
6	2.8102719 ⁽⁺⁷⁾ ₋₅	-67.1	4.1 ^{+0.1} _{-0.1}	11.37 ^{+0.08} _{-0.10}	< 10.2	13.64 ^{+0.01} _{-0.00}	12.64 ^{+0.01} _{-0.01}
7	2.810377 ⁽⁺³⁾ ₋₆	-58.8	10.0 ^{+0.4} _{-0.6}	11.61 ^{+0.09} _{-0.04}	12.57 ^{+0.04} _{-0.02}	13.20 ^{+0.03} _{-0.02}	12.39 ^{+0.03} _{-0.03}
8	2.810579 ⁽⁺⁶⁾ ₋₅	-42.9	4.8 ^{+0.6} _{-0.2}	11.34 ^{+0.10} _{-0.10}	11.79 ^{+0.13} _{-0.19}	13.16 ^{+0.03} _{-0.06}	12.12 ^{+0.06} _{-0.06}
9	2.8106443 ⁽⁺⁴³⁾ ₋₃₀	-37.8	1.8 ^{+0.2} _{-0.3}	11.17 ^{+0.16} _{-0.08}	11.51 ^{+0.25} _{-0.14}	13.15 ^{+0.05} _{-0.04}	12.09 ^{+0.05} _{-0.07}
10	2.810710 ⁽⁺³⁾ ₋₄	-32.7	2.5 ^{+0.3} _{-0.2}	11.17 ^{+0.15} _{-0.17}	12.04 ^{+0.11} _{-0.09}	13.42 ^{+0.04} _{-0.06}	12.25 ^{+0.04} _{-0.09}
11	2.8108055 ⁽⁺⁴⁹⁾ ₋₁₈	-25.1	4.4 ^{+0.4} _{-0.3}	11.79 ^{+0.06} _{-0.05}	12.57 ^{+0.05} _{-0.04}	14.18 ^{+0.03} _{-0.04}	13.01 ^{+0.02} _{-0.05}
12	2.810920 ⁽⁺³⁾ ₋₃	-16.1	4.9 ^{+0.3} _{-0.4}	11.95 ^{+0.07} _{-0.04}	12.66 ^{+0.06} _{-0.04}	14.27 ^{+0.05} _{-0.04}	13.13 ^{+0.04} _{-0.05}
13	2.8110146 ⁽⁺³⁷⁾ ₋₂₇	-8.7	3.7 ^{+0.2} _{-0.2}	11.99 ^{+0.05} _{-0.04}	12.54 ^{+0.04} _{-0.04}	14.05 ^{+0.06} _{-0.04}	12.99 ^{+0.03} _{-0.05}
14	2.8111566 ⁽⁺³⁾ ₋₁₀	2.5	6.1 ^{+0.1} _{-0.2}	12.28 ^{+0.01} _{-0.02}	13.05 ^{+0.01} _{-0.02}	14.64 ^{+0.01} _{-0.01}	13.46 ^{+0.01} _{-0.01}
15	2.8113387 ⁽⁺²⁵⁾ ₋₁₇	16.8	9.5 ^{+0.3} _{-0.2}	12.07 ^{+0.05} _{-0.04}	12.98 ^{+0.01} _{-0.04}	14.55 ^{+0.02} _{-0.02}	13.41 ^{+0.01} _{-0.02}
16	2.811530 ⁽⁺⁸⁾ ₋₅	31.9	14.8 ^{+0.8} _{-0.5}	12.22 ^{+0.04} _{-0.04}	12.70 ^{+0.05} _{-0.04}	14.28 ^{+0.03} _{-0.02}	13.28 ^{+0.02} _{-0.03}
17	2.8117193 ⁽⁺⁸⁾ ₋₉	46.8	3.3 ^{+0.2} _{-0.2}	11.68 ^{+0.05} _{-0.05}	12.33 ^{+0.03} _{-0.03}	13.82 ^{+0.02} _{-0.02}	12.62 ^{+0.03} _{-0.03}
18	2.8118561 ⁽⁺¹⁶⁾ ₋₉	57.5	6.7 ^{+0.2} _{-0.2}	11.82 ^{+0.05} _{-0.05}	12.55 ^{+0.02} _{-0.04}	14.04 ^{+0.02} _{-0.01}	12.94 ^{+0.01} _{-0.02}
19	2.8120187 ⁽⁺¹²⁾ ₋₁₅	70.3	3.5 ^{+0.2} _{-0.2}	11.06 ^{+0.11} _{-0.23}	11.74 ^{+0.13} _{-0.16}	13.64 ^{+0.02} _{-0.02}	12.47 ^{+0.03} _{-0.03}
20	2.8121555 ⁽⁺³²⁾ ₋₁₅	81.1	16.6 ^{+0.2} _{-0.3}	12.28 ^{+0.03} _{-0.05}	12.82 ^{+0.02} _{-0.03}	14.47 ^{+0.01} _{-0.00}	13.36 ^{+0.01} _{-0.01}
21	2.8123923 ⁽⁺¹¹⁾ ₋₁₁	99.7	3.1 ^{+0.1} _{-0.1}	11.53 ^{+0.05} _{-0.05}	11.82 ^{+0.12} _{-0.07}	13.55 ^{+0.01} _{-0.01}	12.44 ^{+0.02} _{-0.02}
22	2.8124936 ⁽⁺¹⁴⁾ ₋₇	107.7	2.3 ^{+0.2} _{-0.2}	11.33 ^{+0.06} _{-0.07}	< 10.3	13.26 ^{+0.01} _{-0.02}	12.27 ^{+0.03} _{-0.01}
23	2.8126321 ⁽⁺⁵⁾ ₋₃	118.6	3.3 ^{+0.1} _{-0.1}	11.34 ^{+0.07} _{-0.06}	11.73 ^{+0.12} _{-0.15}	13.40 ^{+0.00} _{-0.01}	12.43 ^{+0.01} _{-0.01}
24	2.8130940 ⁽⁺³⁴⁾ ₋₁₈	154.9	9.2 ^{+0.1} _{-0.3}	11.76 ^{+0.04} _{-0.04}	12.12 ^{+0.09} _{-0.06}	13.53 ^{+0.01} _{-0.03}	12.57 ^{+0.01} _{-0.05}
25	2.8131968 ⁽⁺¹⁸⁾ ₋₁₆	163.0	2.0 ^{+0.3} _{-0.2}	< 10.2	< 11.2	13.10 ^{+0.03} _{-0.03}	11.88 ^{+0.02} _{-0.09}
26	2.8132860 ⁽⁺¹⁴⁾ ₋₉	170.0	5.2 ^{+0.1} _{-0.2}	11.85 ^{+0.03} _{-0.03}	12.10 ^{+0.07} _{-0.05}	13.72 ^{+0.01} _{-0.01}	12.69 ^{+0.01} _{-0.01}
27	2.8134840 ⁽⁺⁸⁾ ₋₇	185.6	5.9 ^{+0.1} _{-0.2}	11.58 ^{+0.04} _{-0.06}	11.96 ^{+0.09} _{-0.08}	13.69 ^{+0.01} _{-0.00}	12.65 ^{+0.01} _{-0.01}
28	2.8136476 ⁽⁺⁷⁾ ₋₇	198.4	4.8 ^{+0.1} _{-0.1}	11.84 ^{+0.03} _{-0.02}	12.43 ^{+0.03} _{-0.03}	13.92 ^{+0.00} _{-0.01}	12.90 ^{+0.00} _{-0.01}
29	2.8137653 ⁽⁺¹⁷⁾ ₋₁₁	207.7	3.3 ^{+0.3} _{-0.1}	11.28 ^{+0.05} _{-0.12}	11.97 ^{+0.08} _{-0.06}	13.32 ^{+0.02} _{-0.01}	12.34 ^{+0.02} _{-0.03}
30	2.813914 ⁽⁺³⁾ ₋₄	219.4	6.0 ^{+0.3} _{-0.4}	11.67 ^{+0.06} _{-0.03}	< 10.5	13.42 ^{+0.03} _{-0.06}	12.44 ^{+0.06} _{-0.04}
31	2.814043 ⁽⁺²⁾ ₋₃	229.6	7.9 ^{+0.4} _{-0.6}	< 10.3	11.80 ^{+0.26} _{-0.15}	13.79 ^{+0.04} _{-0.03}	12.75 ^{+0.04} _{-0.04}
32	2.814165 ⁽⁺³⁾ ₋₃	239.1	7.0 ^{+0.5} _{-0.3}	11.69 ^{+0.04} _{-0.07}	< 10.3	13.81 ^{+0.03} _{-0.04}	12.73 ^{+0.03} _{-0.05}
33	2.8143106 ⁽⁺²⁵⁾ ₋₂₄	250.6	5.6 ^{+0.3} _{-0.1}	11.69 ^{+0.05} _{-0.04}	11.87 ^{+0.10} _{-0.12}	13.59 ^{+0.03} _{-0.01}	12.60 ^{+0.02} _{-0.03}
34	2.8144455 ⁽⁺¹²⁾ ₋₉	261.2	3.8 ^{+0.2} _{-0.1}	11.57 ^{+0.04} _{-0.06}	12.04 ^{+0.05} _{-0.07}	13.34 ^{+0.01} _{-0.01}	12.39 ^{+0.02} _{-0.01}
35	2.8146554 ⁽⁺⁹⁾ ₋₄	277.7	8.0 ^{+0.1} _{-0.1}	11.60 ^{+0.06} _{-0.05}	12.46 ^{+0.03} _{-0.03}	13.51 ^{+0.00} _{-0.00}	12.56 ^{+0.01} _{-0.01}
$\log N_{\text{tot}}$	13.25 ^{+0.01} _{-0.01}	13.86 ^{+0.01} _{-0.01}	15.43 ^{+0.00} _{-0.00}	14.33 ^{+0.00} _{-0.00}
$[\text{X}/\text{H}]^\ddagger$	-0.68 ^{+0.01} _{-0.01}	-1.15 ^{+0.01} _{-0.01}	-1.44 ^{+0.01} _{-0.01}	-1.26 ^{+0.01} _{-0.01}
$[\text{X}/\text{Zn II}]^\ddagger$	0.00 ^{+0.01} _{-0.01}	-0.47 ^{+0.01} _{-0.01}	-0.76 ^{+0.01} _{-0.01}	-0.57 ^{+0.01} _{-0.01}

† Velocity offset relative to $z = 2.811124$.‡ Using solar abundances from [Asplund et al. \(2009\)](#).